Is $Ba_3In_2O_6$ a high-T_c superconductor?

To cite this article: F V E Hensling *et al* 2024 *J. Phys.: Condens. Matter* **36** 315602

OPEN ACCESS
IOP Publishing
Journal of Physics: Condensed Matter
J. Phys.: Condens. Matter **36** (2024) 315602 (14pp)
https://doi.org/10.1088/1361-648X/ad42f3

Is $Ba_3In_2O_6$ a high-T_c superconductor?

F V E Hensling[1,2,*], D Dahliah[3,4,††], M A Smeaton[1], B Shrestha[5,6], V Show[7], C T Parzyck[8], C Hennighausen[8], G N Kotsonis[1], G-M Rignanese[3], M R Barone[7], I Subedi[5,6], A S Disa[9,10], K M Shen[8,10], B D Faeth[7], A T Bollinger[11], I Božović[11,12,13], N J Podraza[5,6], L F Kourkoutis[9,10,†], G Hautier[3,14] and D G Schlom[1,10,15]

[1] Department of Materials Science and Engineering, Cornell University, Ithaca, NY 14853, United States of America
[2] Max Planck Institute for Solid State Research, Heisenbergstraße 1, 70569 Stuttgart, Germany
[3] Institute of Condensed Matter and Nanosciences, Université catholique de Louvain, 1348 Louvain-la-Neuve, Belgium
[4] Department of Physics, An-Najah National University, Nablus, Palestine
[5] Department of Physics and Astronomy, University of Toledo, Toledo, OH 43606, United States of America
[6] Wright Center for Photovoltaic Innovation and Commercialization, University of Toledo, Toledo, OH 43606, United States of America
[7] Platform for the Accelerated Realization, Analysis, and Discovery of Interface Materials (PARADIM), Cornell University, Ithaca, NY 14853, United States of America
[8] Laboratory of Atomic and Solid State Physics, Cornell University, Ithaca, NY 14853, United States of America
[9] School of Applied & Engineering Physics, Cornell University, Ithaca, NY 14853, United States of America
[10] Kavli Institute at Cornell for Nanoscale Science, Ithaca, NY 14853, United States of America
[11] Brookhaven National Laboratory, Upton, NY 11973, United States of America
[12] Department of Chemistry, Yale University, New Haven, CT 06520, United States of America
[13] Energy Sciences Institute, Yale University, West Haven, CT 06516, United States of America
[14] Thayer School of Engineering, Dartmouth College, Hanover, NH 03755, United States of America
[15] Leibniz-Institut für Kristallzüchtung, Max-Born-Strasse 2, 12849 Berlin, Germany

E-mail: hensling@cornell.edu

Received 24 January 2024, revised 31 March 2024
Accepted for publication 24 April 2024
Published 9 May 2024

Abstract

It has been suggested that $Ba_3In_2O_6$ might be a high-T_c superconductor. Experimental investigation of the properties of $Ba_3In_2O_6$ was long inhibited by its instability in air. Recently epitaxial $Ba_3In_2O_6$ with a protective capping layer was demonstrated, which finally allows its electronic characterization. The optical bandgap of $Ba_3In_2O_6$ is determined to be 2.99 eV in-the (001) plane and 2.83 eV along the *c*-axis direction by spectroscopic ellipsometry. First-principles calculations were carried out, yielding a result in good agreement with the experimental value. Various dopants were explored to induce (super-)conductivity in this otherwise insulating material. Neither *A*- nor *B*-site doping proved successful. The underlying reason is predominately the formation of oxygen interstitials as revealed by scanning

† Deceased.
†† Publisher's note. Whilst IOP Publishing adheres to and respects UN resolutions regarding the designations of territories (available at www.un.org/press/en), the policy of IOP Publishing is to use the affiliations provided by its authors on its published articles.
* Author to whom any correspondence should be addressed.

transmission electron microscopy and first-principles calculations. Additional efforts to induce superconductivity were investigated, including surface alkali doping, optical pumping, and hydrogen reduction. To probe liquid-ion gating, $Ba_3In_2O_6$ was successfully grown epitaxially on an epitaxial $SrRuO_3$ bottom electrode. So far none of these efforts induced superconductivity in $Ba_3In_2O_6$, leaving the answer to the initial question of whether $Ba_3In_2O_6$ is a high-T_c superconductor to be 'no' thus far.

Supplementary material for this article is available online

Keywords: high-T_c superconductivity, first-principles calculations, molecular-beam epitaxy

1. Introduction

Since the discovery of superconductivity [1] there has been a relentless drive to find materials with higher transition temperature (T_c) to broaden technological applications of superconductors. Without a doubt the most significant discovery in this regard is high-T_c superconductivity in cuprates [2]. It is no surprise that the desire to find new and better superconductors was accompanied by countless efforts to predict suitable candidate materials. When these efforts first evolved Matthias dismissed them as futile and highlighted the benefits of an empirical approach [3–5]. In fact, the discovery of (unconventional) superconductors remains highly empirical to this day. This is despite the impressive developments in the prediction of materials properties [6].

Recently, a novel approach to predict superconductors has emerged. Machine learning utilizes huge materials databases to compare known superconducting materials and identify materials with similar structures not yet identified as superconductors [7–9]. One of the most exciting materials this approach has predicted is $Ba_3In_2O_6$. It is not a direct derivative of a known high-T_c superconductor and the predicted T_c is fairly high at 78.0 K [7]. The suggestion that this material might be a high-temperature superconductor actually dates back to the first report of high-quality single crystals of $Ba_3In_2O_6$ [10]. This supposition elicited from human intelligence through recognition that its structure (see figure 1), which is closely related to $Sr_3Ti_2O_7$, is isostructural to the known high-T_c superconductor $La_2SrCu_2O_6$ [10–12].

Previously, the hygroscopic nature of $Ba_3In_2O_6$ and the resulting instability in air prohibited the electrical characterization of $Ba_3In_2O_6$ powders and small single crystals that were about 0.1 mm in size [10, 13, 14]. The synthesis of epitaxial thin films of $Ba_3In_2O_6$ has obvious advantages for testing the electrical transport properties of $Ba_3In_2O_6$ but faces additional challenges. To start with, the large *a*-axis lattice constant (0.419 nm) of $Ba_3In_2O_6$ suggests a limited choice of substrates and its high formation temperature pushes the limits of conventional heaters [13–16]. Recently, we developed a means to grow single-phase films of $Ba_3In_2O_6$ utilizing suboxide molecular-beam epitaxy (s-MBE) [14, 17]. The large *a*-axis lattice constant of $Ba_3In_2O_6$ is not far from that of (001) MgO, a substrate of industrial relevance and commercial availability [18–22]. While a perovskite substrate with a large lattice constant would provide a more suitable epitaxial template, there are none commercially available close in size. Nonetheless, epitaxial films of reasonable quality were grown on MgO [14]. We further showed that these epitaxial layers can be stabilized by capping with amorphous SiO_2 [14]. This development opens the door to, in this work, finally characterize the electronic properties of $Ba_3In_2O_6$ and answer the question whether it is a high-T_c superconductor.

2. Method

2.1. Film growth

All epitaxial films were grown in a Veeco Gen10 MBE. Epitaxial $Ba_3In_2O_6$ films were grown with a Ba-flux of $\approx 5.1 \times 10^{13}$ Ba/(cm^2 s), and an In_2O-flux of $\approx 2.2 \times 10^{13}$ In_2O/(cm^2 s) resulting in a growth rate of 2 nm min^{-1}. The films were capped with amorphous SiO_2. Details of epitaxial $Ba_3In_2O_6$ film growth and capping are described in [14]. In brief, the amorphous SiO_2 capping layers were deposited from a molecular beam of SiO (flux of 1×10^{13} SiO/(cm^2 s)) emanating from an effusion cell containing chunks of amorphous SiO in a background pressure of 5×10^{-7} Torr of a mixture of $\sim$10% ozone and 90% oxygen with the substrate temperature at $\leqslant$350 °C. Some samples were prepared on underlying epitaxial $SrRuO_3$ electrode layers, grown by the means described in [23]. Ce, La, and Sb were evaporated from elemental sources. The SnO, and W_3O_9 suboxide molecular beams were obtained from heating SnO_2 and WO_3, respectively [17, 24]. All fluxes were roughly estimated by a quartz-crystal microbalance and refined by the subsequent growth of binary oxide calibration layers [25]. The respective flux ranges Φ were: $\Phi_{Ce} \leqslant 2.5 \times 10^{12}$ Ce/(cm^2 s), $\Phi_{La} \leqslant 1.1 \times 10^{13}$ La/(cm^2 s), $\Phi_{Sb} \leqslant 2.2 \times 10^{12}$ Sb/(cm^2 s), $\Phi_{SnO} \leqslant 1.1 \times 10^{13}$ SnO/(cm^2 s), $\Phi_{W3O9} \leqslant 0.7 \times 10^{12}$ W_3O_9/(cm^2 s). (001) MgO substrates were supplied by CrysTec GmbH, and (001) $SrTiO_3$ substrates were supplied by Shinkosha Co. Ltd and prepared as described by Koster *et al* [26, 27]. Film growth was monitored *in situ* by reflection high-energy electron diffraction (RHEED). Unless stated otherwise, films were capped by amorphous SiO_2 and grown on (001) MgO substrates.

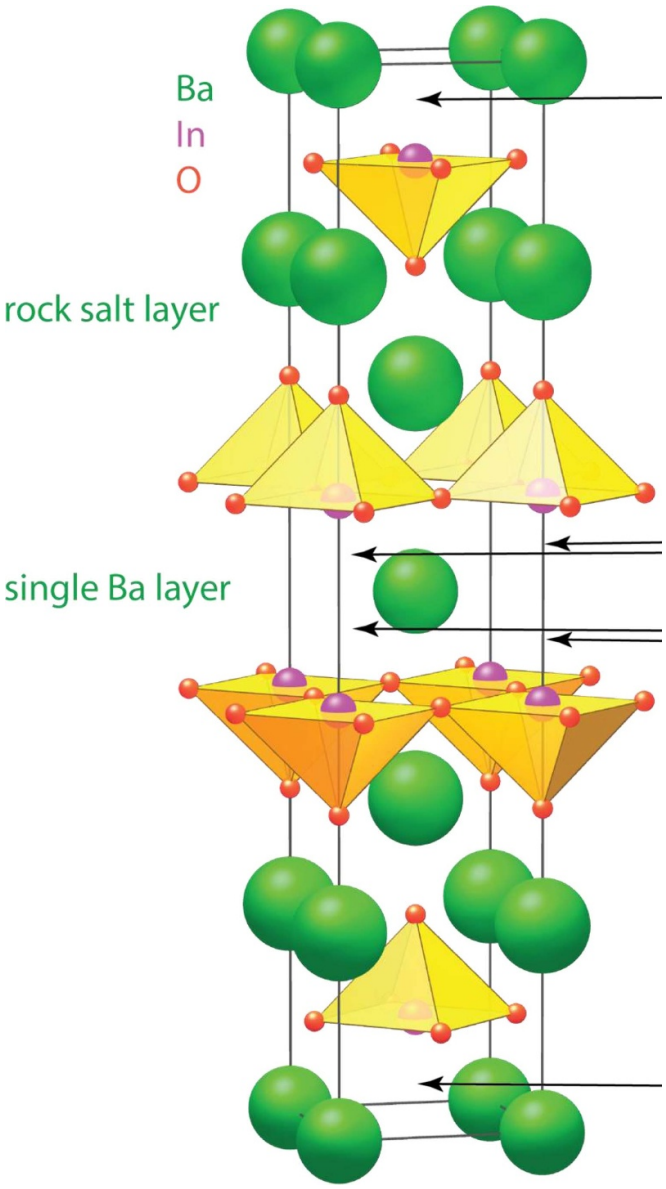

Figure 1. Structure of $Ba_3In_2O_6$ with Ba depicted in green, In in violet, O in red, and the O-octahedra in yellow. The easy interstitial sites resulting from the fivefold coordination of In are for some examples marked by black arrows.

2.2. Characterization

X-ray diffraction (XRD) measurements were obtained with a Panalytical Empyrean with Cu-$K_{\alpha 1}$ radiation. Cross-sectional scanning transmission electron microscopy (STEM) specimens were prepared using a Thermo Fisher Scientific Helios G4UX focused ion beam (FIB) using standard liftout and thinning methods. High-angle annular dark-field (HAADF) and annular bright field (ABF)-STEM data were acquired using a Thermo Fisher Scientific Spectra 300 X-CFEG operating at 300 kV with a convergence angle of 30 mrad. Inner and outer collection angles for HAADF and ABF imaging were approximately 60 and 200 mrad and 15 and 30 mrad, respectively. Energy dispersive x-ray spectroscopy (EDX) maps were acquired with a Super-X EDX detector, and electron energy loss spectroscopy (EELS) maps were acquired with a Gatan Continuum system equipped with a scintillator CMOS camera. STEM specimens were stored in a vacuum chamber between FIB preparation and imaging to minimize air exposure.

Spectroscopic ellipsometry was performed at room temperature using a single rotating compensator multichannel ellipsometer (M-2000 FI, J.A Woolam, Co. Inc.) [28, 29]. Ellipsometric spectra were collected at 50° and 60° angles of incidence over a photon energy range of 0.735–5.887 eV and fit via iterative least-square regression using a structural and optical model, which minimizes the unweighted error function or mean square error [30] to extract the complex dielectric function ($\varepsilon = \varepsilon_1 + i\varepsilon_2$) spectra and structural properties such as layer thicknesses. Spectra in ε of MgO and amorphous SiO_2 layers were obtained from parametric models fitted to ellipsometric spectra obtained from a bare (001) MgO substrate and a separate amorphous SiO_2 film directly deposited on a (001) MgO substrate, respectively.

Spectra in ε of the bare MgO substrate were described with a Sellmeier expression [31] and a constant additive term to ε_1 (ε_∞) with a structural model consisting of semi-infinite MgO surface roughness. A surface roughness layer 2.13 ± 0.05 nm thick was obtained from the fit using the Bruggeman effective medium approximation (EMA) [32] consisting of equal fractions of MgO and void to describe spectra in ε for surface roughness. This surface roughness layer thickness was fixed to represent that of the physically mixed interfacial layer for all films deposited on MgO, and spectra in ε for the respective physically mixed layers consist of equal material fractions of MgO and the film. The spectra in ε of the amorphous SiO_2 layer were obtained from a model consisting of the semi-infinite MgO substrate, a 0.5 MgO + 0.5 amorphous SiO_2 EMA layer, the amorphous SiO_2 film, and surface roughness. Spectra in ε of amorphous SiO_2 are represented by a Tauc–Lorentz oscillator [33], Sellmeier expression, and ε_∞. The amorphous SiO_2 thickness is 54.0 ± 0.3 nm and surface roughness consisting of equal parts amorphous SiO_2 and void is 5.3 ± 0.1 nm thick. A distinct interface layer with a unique set of optical properties common in all samples was also observed between epitaxial thin films and amorphous SiO_2. The spectra in ε and thickness of this layer were initially obtained using a parametric expression consisting a Lorentz oscillator [31] and ε_∞, incorporated between the epitaxial thin film and amorphous SiO_2 layer of the undoped $Ba_3In_2O_6$ sample. This spectrum in ε was then used to obtain the thickness of this interfacial layer in the doped epitaxial thin film samples.

The structural model for each epitaxial thin film sample consists of the semi-infinite MgO substrate, a 0.5 MgO + 0.5 epitaxial thin film EMA layer, the epitaxial thin film layer, the interface layer, the amorphous SiO_2 capping layer, the amorphous SiO_2 surface roughness, and air ambient. The surface roughness here was described by an EMA of amorphous SiO_2 and a variable void fraction. All doped and undoped epitaxial thin films exhibit structural and optical anisotropy with the optic axis perpendicular to the sample surface. Spectra in ε were defined separately for electric fields oscillating normal to (in-plane) and parallel to (out-of-plane) the optic axis for each epitaxial thin film. Spectra in ε_2 in each direction for all

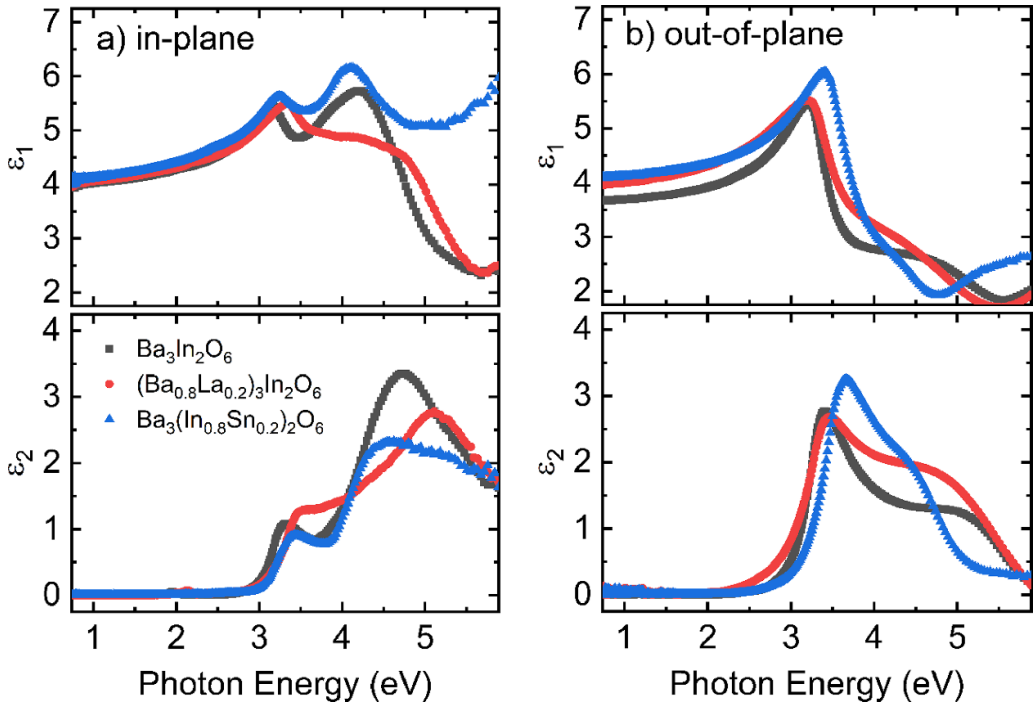

Figure 2. Numerically inverted spectra in ε for (a) in-plane and (b) out-of-plane directions of epitaxial doped and undoped $Ba_3In_2O_6$ films on MgO. For the in-plane direction, the transition strength of the critical points at energies >4.5 eV is substantially suppressed for both doped films. For the out-of-plane direction, the Sn-doped epitaxial film has a slight blue shift of the lowest energy critical point with increased transition strength compared to other epitaxial samples whereas the second-lowest critical point is red shifted. For the La-doped sample, both critical point features are located at approximately the same energies as undoped $Ba_3In_2O_6$, but with differences in transition strength and broadness of the features at higher photon energies.

doped and undoped epitaxial films were described by critical point parabolic band (CPPB) oscillators [32] above the lowest energy critical point to describe above gap electronic transitions and an Urbach tail starting at the lowest energy critical point to describe sub-gap absorption [34]. The fit parameters of the CPPB oscillators are critical point resonance energy (E_n), amplitude (A_n), critical point broadening (Γ_n), and the phase projection factor (φ_n). Critical point dimensionality was fixed at $\mu = 1$ for excitonic transitions for simplicity. Spectra in ε_1 were described by Kramers–Kronig integration [31] of the respective ε_2 spectra along with Sellmeier expressions and ε_∞. For Sellmeier expressions, fit parameters are a resonance energy (E_s) outside the measured spectral range and an amplitude (A_s). Initially, the parametric model for the undoped $Ba_3In_2O_6$ sample was developed and values for the fit parameters were obtained. φ_n values of the CPPB oscillators from undoped $Ba_3In_2O_6$ were taken as reference and fixed for the other doped samples corresponding to the critical points at approximately similar resonance energies along each direction. Any other features present in doped samples were modeled by adding CPPB oscillators, the φ_n values of which were also fitted. Fit parameters describing spectra in ε and structural parameters are listed in supplementary tables 1–3. After obtaining layer thicknesses from the parametric fit, numerical inversion [35] was then performed to determine spectra in ε for each direction from the measured ellipsometric spectra using fixed thicknesses and parametric spectra in ε for the orthogonal direction and all other layers.

Absorption coefficient (α) spectra of each direction of all epitaxial layers was obtained from

$$\alpha = 4\pi k/\lambda,$$

where λ is the photon wavelength and k is the extinction coefficient obtained from numerically inverted

$$\varepsilon = (n + ik)^2.$$

The direct optical bandgap in each direction was calculated using Tauc plots [36] of the respective α^2 as a function of photon energy and extrapolating to the photon energy where $\alpha^2 = 0$. Bandgap energies, lowest energy critical points, Urbach energies, and the range of α extrapolated for the Tauc plots in each direction of each sample are in supplementary tables 1–4; numerically inverted spectra in ε are in figure 2.

2.3. *First-principles calculations*

Density functional theory adopting the projector augmented wave method [37], as implemented in the Vienna *ab initio* simulation package [38, 39], was used to calculate the electronic structure and the formation energy of point defects. The wave functions were expanded on a plane-wave basis set employing a cut-off energy of 520 eV. The atomic coordinates and the vector lattice were fully optimized when computing bulk properties including band gap. Point defects were studied using the supercell approach using a fixed volume [40]. The

different atomic models were generated utilizing the Python Charge Defects Toolkit (PyCDT) [41] using a supercell of 88 atoms. The Brillouin zone was sampled using a Γ only k-point grid. The exchange–correlation potential was obtained through adopting the Heyd–Scuseria–Ernzerhof (HSE) hybrid functional with an exact-exchange fraction of 0.25 and a screening length of 0.2 Å [42, 43]. Spin-polarized calculations were performed, and all supercells were relaxed at fixed volume until the forces on the ions were smaller than 0.1 eV $Å^{-1}$. The occupation of the electronic states was determined through the Gaussian smearing method with a smearing width of 0.05 eV. The formation energy of each charged-defect state was computed as a function of the Fermi level E_f as [44, 45]

$$E_{\text{form}}\left[X^q, E_f\right] = E_{\text{tot}}\left[X^q\right] - E_{\text{tot}}^{\text{bulk}} - \sum n_i\mu_i + qE_f + E_{\text{corr}},$$

where $E_{\text{tot}}\left[X^q\right]$ and $E_{\text{tot}}^{\text{bulk}}$ are the total energies of the defective supercell (for a given defect X in the charge state q) and the bulk energy, respectively. The third term represents the energy needed to exchange atoms with thermodynamic reservoirs, where n_i indicates the number of atoms of the species i removed or added to create the defect, and μ_i are the corresponding chemical potentials [46]. We computed the phase diagram of Ba–In–O with different possible dopants at 0 K at the same level of theory and determined the limits of the allowed chemical potential of these species. The fourth term represents the energy to exchange electrons with the host material through the electronic chemical potential which is the Fermi energy level E_f. Finally, the last term in the equation is a correction accounting for the finite size of the supercell. Here, we used the extended Freysoldt's (Kumagai's) scheme [40, 47].

The thermodynamic transition state of defect X from state q_1 to q_2, which corresponds to the energetic level at which a defect captures (or emits) a free carrier, is defined as the position of the Fermi level at which the defect formation energy of both states q_1 and q_2 are equal ($E_{\text{form}}\left[X^{q_1}, E_f\right] = E_{\text{form}}\left[X^{q_2}, E_f\right]$). The transition level, $\epsilon\left(q_1/q_2\right)$, relative to the VBM ($E_f = E_{\text{VBM}}$) is

$$\epsilon\left(q_1/q_2\right) = \frac{E_{\text{form}}\left[X^{q_2}, E_{\text{VBM}}\right] - E_{\text{form}}\left[X^{q_1}, E_{\text{VBM}}\right]}{q_2 - q_1}.$$

3. Results

Probing an as-grown $Ba_3In_2O_6$ film by a simple four-point measurement quickly reveals its insulating behavior. To understand how insulating $Ba_3In_2O_6$ is, we determine its bandgap by spectroscopic ellipsometry.

Supplementary figure 1 shows the spectra in ε of the (a) amorphous SiO_2 capping layer, (b) interface layer, and (c) semi-infinite MgO substrate. Comparison of ε_1 obtained here for MgO matches well with that previously reported [48] with slightly higher values of ε_1 at low photon energies and slightly lower values at high photon energies when compared to the reference spectra. For amorphous SiO_2, the Tauc-gap is obtained at 2.40 ± 0.02 eV which is lower than the bandgap energies reported for material closer to stoichiometric amorphous SiO_2 [49]. This difference for the molecular-beam deposited amorphous SiO_2 is attributed to oxygen vacancies forming electron trap states which lead to absorption peaks in the 5–7 eV region depending on the extent of oxygen vacancies present in the amorphous film [50].

The direct optical bandgaps obtained for the undoped $Ba_3In_2O_6$ are 2.990 ± 0.006 eV for in-plane and 2.826 ± 0.005 eV for out-of-plane directions as shown in figure 2 (extrapolation in supplementary figure 2). The optical bandgap can be considered the lowest value observed. Hence, the direct optical bandgap of undoped $Ba_3In_2O_6$ is 2.826 ± 0.005 eV. From first-principles defect computations using the HSE functional we determine a direct gap of 2.8 eV and an indirect gap of 2.15 eV (see figure 5(a)). The computed bandgap, thus, agrees well with the experimental value and is within the typical errors between HSE and the experiment [51]. This precision shows that HSE hybrid computations are well suited for studying dopant levels in $Ba_3In_2O_6$.

3.1. A-site doping of $Ba_3In_2O_6$

Given the insulating behavior in undoped epitaxial $Ba_3In_2O_6$, the obvious next step in trying to induce (super-) conductivity is to dope the system. A substitution of the A-site cation with La was previously successful for the structural equivalent homologous $Sr_{n+1}Ti_nO_{3n+1}$ RP series and for $BaSnO_3$ [52–54]. It, thus, constitutes a reasonable starting point.

We achieve this by successively decreasing the Ba flux and applying a La flux to compensate that decrease. The doping concentrations given in the following, thus, refer to the percentage of flux that was substituted. Figure 3(a) shows the evolution of the $(Ba_{1-x}La_x)_3In_2O_6$ θ–2θ diffraction pattern with an increase of the La-doping concentration. For 10% La-doping (teal) no secondary phases are notable but a shift of the peaks to higher 2θ values is observed. Increasing the La-concentration further to 20% (purple) results in a further shift of the diffraction angles of the film to higher 2θ values and the formation of a Ba-poor secondary phase becomes barely visible [14]. We, thus, conclude the solubility limit of La in $Ba_3In_2O_6$ to be approximately 20%. The maintenance of excellent structural quality is corroborated by the HAADF STEM image in figure 3(b) of the 20% La-doped epitaxial $Ba_3In_2O_6$. It is of comparable quality to previously reported undoped films [14]. The shift of the diffraction peaks to higher 2θ values with increasing La-concentration is in good agreement with the substitution of Ba^{2+} by La^{3+}. As given in table 1, the ionic radius of La^{3+} is smaller than that of Ba^{2+} [55] resulting in a lattice compression and, thus, a shift of the diffraction peaks to higher 2θ values.

The EELS spectra in figures 4(b) and (c), which correspond to the ADF image in (a), reveal that: (1) As indicated by the θ–2θ diffraction patterns, La substitutes Ba. (2) La solely substitutes for the Ba located on the single layer. This is schematically depicted in figure 4(d).

Despite the ability to substitute significant amounts of Ba^{2+} by La^{3+} a simple four-point measurement still reveals highly insulating behavior. We, thus, next probe the bandgap for

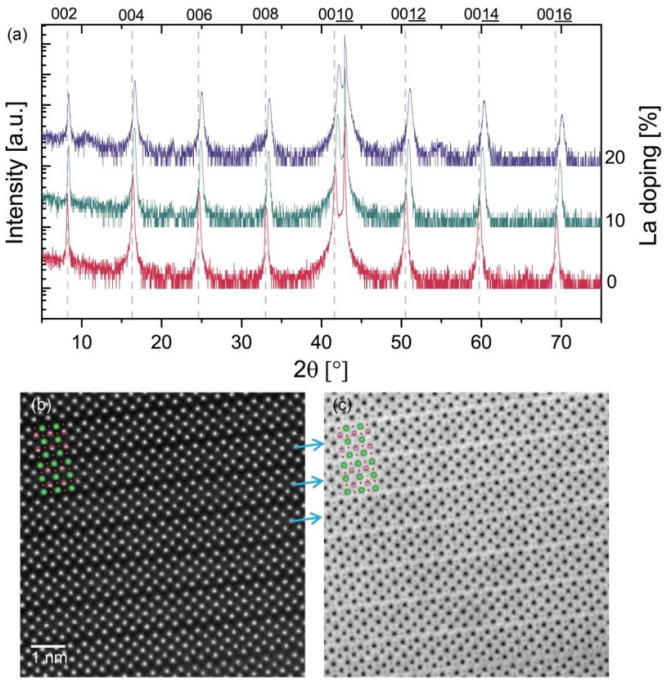

Figure 3. (a) θ–2θ diffraction patterns of ≈160 nm thick epitaxial $Ba_{3-x}La_xIn_2O_6$ with $x = 0$ (red), $x = 0.3$ (teal), and $x = 0.6$ (purple). With increasing doping, the film peaks shift to larger 2θ values which is most easily observed at the 00$\underline{16}$ peak. The dashed lines mark the peak positions for *c*-axis oriented bulk $Ba_3In_2O_6$ as reported by Antipov et al [15]. (b) HAADF STEM image of the 20% La-doped sample and (c) simultaneously acquired ABF STEM image revealing additional oxygen in the single *A*-site layer marked by the blue arrows. A schematic unit cell is overlaid onto the ABF image with green representing the *A*-site cations, magenta the *B*-site cations, and red representing oxygen.

Table 1. Ionic radii of the cations in the parent compound (top two rows) and the dopants considered. Values adapted from [55].

Coordination No.	Ion	Eff. Ionic radius (pm)
VIII	Ba^{2+}	142
IX	Ba^{2+}	147
V	In^{3+}	71[a]
VIII	La^{3+}	116
IX	La^{3+}	122
V	Sn^{2+}	118
V	Sn^{4+}	62

[a] The value for fivefold coordinated In^{3+} is approximated from the fourfold and sixfold coordinated In^{3+} values.

a 20% La-doped epitaxial $Ba_3In_2O_6$ film by spectroscopic ellipsometry. Figure 2 shows the measured bandgap (a) in-plane and (b) out-of-plane. The bandgap in the in-plane direction is insignificantly increased when compared to that of the undoped film (3.057 ± 0.005 eV). The out-of-plane bandgap is slightly decreased (2.614 ± 0.006 eV). The extrapolation can be found in supplementary figure 3. As the bandgap is considered the lowest value observed, 20% La-doping results in a lowering of the bandgap by ≈0.21 eV.

To shed light on the lack of conductivity despite the lowered bandgap and the significant incorporation of La^{3+} on the Ba^{2+}-site, we utilize first-principles defect computations using the HSE functional. Figure 5 shows the formation energy of different neutral (horizontal lines) and charged (positive slope for a positive charge and negative slope for a negative charge with respect to the regular charge of the site) defects in La-doped $Ba_3In_2O_6$ for cation-rich and oxygen-poor conditions (other conditions found in supplementary figure 4). Cation-rich and oxygen-poor conditions should favor n-type doping. We first consider the defect formation energies for different substitution sites for La. Two different formation energies for La^{3+} are observed for the two different Ba^{2+}-sites to be occupied. A substitution on the rock salt site (brown) shows a higher formation energy than on the single layer site (olive) and is even higher than the substitution of La^{3+} for In^{3+} (grey). This is in good agreement with the experimental observations. The transition state between the neutral 2+ state and the 3+ state of La on the single layer site is located 0.11 eV below the bandgap. It is thus shallow enough to potentially bring carriers especially when high levels of La substitute to Ba.

The reason for the lack of conductivity can nevertheless be elucidated with these defect computations—through a compensation effect. The fivefold coordination of In leaves an easy interstitial site to fill (see figure 1 black arrows). An oxygen occupation of this interstitial is represented in light blue in figure 5. It is apparent that an occupation of the interstitial with oxygen in the 2-state is energetically favorable in the presence of La^{3+}, even for the oxygen-poor conditions assumed. Any potential electron doping is, thus, compensated by the oppositely charged oxygen interstitials. Astonishingly, these oxygen interstitials can be experimentally observed. The ABF in figure 3(c) reveals additional oxygen at the expected positions marked by the blue arrows.

In addition to La, Ce was attempted as a dopant due to its successful utilization in high-T_c superconducting cuprates [56]. The behavior of Ce-doped $Ba_3In_2O_6$ was, as far as tested, identical to that of La-doped $Ba_3In_2O_6$. While La doping of $Ba_3In_2O_6$ did not result in the desired (super-) conductivity, the excellent agreement between first-principles defect computations and experimental observations are notable, especially the observation of oxygen interstitials compensating the La-doping.

3.2. *B*-site doping of $Ba_3In_2O_6$

While *B*-site doping in cuprate high-T_c superconductors typically rapidly destroys the superconductivity due to the 2D oxygen-copper plane-based conduction mechanism, *B*-site doping is what led to the discovery of superconductivity in bismuth oxide-based superconductors in the first place [57–59]. We can draw inspiration for a promising dopant for the In-site from one of the most relevant oxide conductors, Sn-doped In_2O_3 (ITO) [60].

We achieve Sn-doping by successively decreasing the In_2O flux and increasing the SnO flux accordingly. Figure 6(a) shows the θ–2θ-scan of a 20% Sn-doped sample (green) in comparison to the same stoichiometric sample (red) as shown

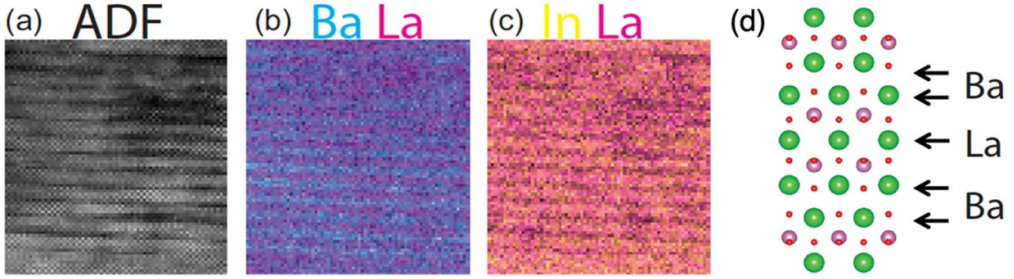

Figure 4. (a) Simultaneously acquired cross-sectional ADF STEM image and (b)–(c) EELS maps of a 20% La-doped $Ba_3In_2O_6$ film, where blue represents Ba, magenta La, and yellow In. It is revealed that La does not occupy the In-sites and sits on the single plane Ba-site. This is schematically depicted in (d) with green representing the *A*-site cations, magenta the *B*-site cations, and red representing oxygen (compare figure 1).

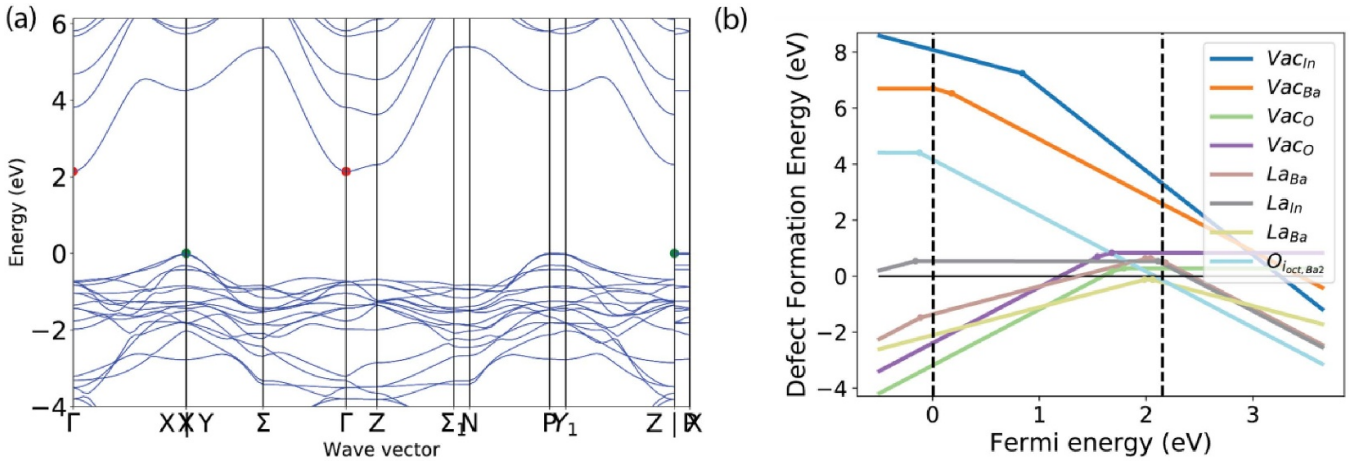

Figure 5. (a) Density of states of undoped $Ba_3In_2O_6$ obtained by HSE computations revealing a direct gap of 2.8 eV and an indirect gap of 2.15 eV. (b) Dependence of the defect formation energy on the Fermi energy for cation-rich and oxygen-poor growth conditions obtained by HSE computations for La-doping. The two different formation energies for the substitution of Ba by La result from the two different Ba-sites. Brown represents the rock salt site and light green the single layer site. The substitution of La for In is shown in grey. Violet represents the formation of an oxygen vacancy in the rock salt layers and green in the single layers. Orange represents Ba vacancies, dark blue In vacancies, and light blue the formation of oxygen interstitials.

in figure 3(a). 20% Sn-doping results in no additional peaks and the sharp peaks of the undoped sample are preserved. Zooming in on the 00$\underline{16}$ peak (figure 6(b)) reveals a peak shift to lower 2θ angles. The maintenance of high structural quality is also confirmed by the HAADF image in figure 6(c). There is no notable difference between the image of 20% Sn-doped $Ba_3In_2O_6$ in figure 6(c) and undoped epitaxial $Ba_3In_2O_6$ films in the literature [14]. Attempting higher percentages of Sn incorporation results in phase separation, while lower percentages are possible, the results from such films are comparable. Here, we focus on 20% Sn-doped samples because the effects described are most apparent for these films.

The peak shift to lower angles observable for 20% Sn-doping in figure 6(b) is surprising as we expect Sn to be in its more stable 4+ oxidation state. Considering table 1, Sn^{4+} has a smaller ionic radius than In^{3+} [55]. Thus, a peak shift in the opposite direction, i.e. to higher angles is expected.

To ensure the incorporation of Sn on the In-site we utilize EDX as Sn and In cannot be distinguished by EELS. Figure 7(a) shows a wider field of view of figure 6(c). Figures 7(b) and (c) show EDX elemental maps with atomic resolution of that same section for In and Ba, respectively. The signal-to-noise ratio in the Sn map in figure 7(d) is too small to draw any conclusions. Nonetheless, a line profile along the blue line in figure 7(a) reveals the Sn substitution site. Figures 7(e) and (f) clearly show that the Sn-signal follows that of the In-signal and is opposite to that of the Ba-signal.

Considering the perfect structure revealed by XRD and HAADF and the distribution of Sn by EDX, it is clear that Sn is incorporated on the *B*-site of the epitaxial $Ba_3In_2O_6$ films. The peak shift to lower 2θ values can, thus, only be explained by a substitution of In^{3+} by Sn^{2+}. In contrast to the smaller ionic radius of Sn^{4+}, the ionic radius of Sn^{2+} is larger than that of In^{3+} (see table 1) and explains a shift to lower angles in 2θ. For obvious reasons we do not expect electron doping when substituting In^{3+} by Sn^{2+}. However, p-type doping as observed in cuprates is feasible for such a substitution [61]. Nonetheless, a four-point measurement quickly reveals the absence of any conductivity. Spectroscopic ellipsometry further reveals no significant change in the bandgap: 2.900 ± 0.006 eV (supplementary figure 5).

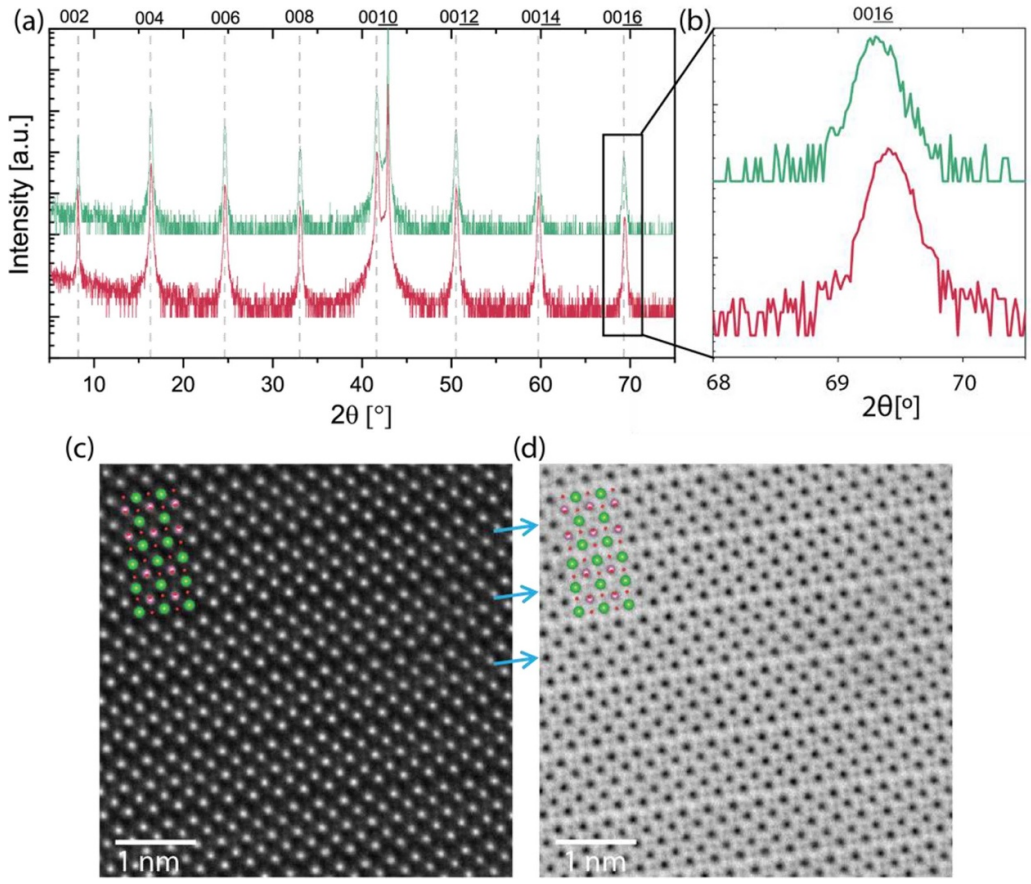

Figure 6. (a) θ–2θ diffraction patterns of ≈160 nm thick epitaxial $Ba_3In_{2-x}Sn_xO_6$ with $x = 0$ (red) and $x = 0.4$ (green). The shift of the film peaks to smaller 2θ values is most easily observed for the 00$\underline{16}$ peak (b). The dashed lines mark the peak positions for *c*-axis oriented bulk $Ba_3In_2O_6$ as reported by Antipov *et al* [15]. (c) HAADF-STEM image of the 20% Sn-doped sample and (d) simultaneously acquired ABF STEM image revealing additional oxygen in the single *A*-site layer marked by the blue arrows. A schematic unit cell is overlaid on the ABF image with green representing the *A*-site cations, magenta the *B*-site cations, and red representing oxygen (same colour scheme as figure 1).

Given the precision of first-principles defect computations using the HSE functional and experimental results, thus far, it is intriguing to probe whether light can be shed on the unusual Sn^{2+} state in 20% Sn-doped $Ba_3In_2O_6$. Figure 8 shows the formation energy of different defects in Sn-doped $Ba_3In_2O_6$ for cation-rich and oxygen-poor conditions (other conditions are found in supplementary figure 6). As for the La defect and as expected, the oxygen interstitial site is also compensating n-type doping as observed experimentally in figure 6(d). The Sn on In defect can be low in energy in agreement with the high concentration of Sn incorporated experimentally in $Ba_3In_2O_6$. The Sn_{In} (+1/0) is, however, slightly deeper than La_{Ba} (+1/0). Interestingly, when the Fermi level is pushed towards the conduction band −1 defect state is favored and will correspond to a +2 oxidation state for Sn in agreement with the experimental evidence. We note that the Sn_{In} (0/−1) is far from the valence band edge making Sn^{2+} not an option for p-type doping.

As other potential *B*-site dopants, W and Sb were attempted as both are well-known dopants for In_2O_3 [62, 63]. However, it was not possible to incorporate either one successfully. In terms of achieving (super-)conductivity Sn-doping proved equally as futile as La-doping. Yet again the underlying defect chemistry turned out to be intriguing. The usually difficult to stabilize Sn^{2+} [64] is readily stabilized when doping $Ba_3In_2O_6$ with Sn.

3.3. *Alternative strategies to induce superconductivity*

As neither *A*-site nor *B*-site doping with the obvious dopants proved successful, the next step was to turn to different approaches to induce superconductivity.

3.3.1. Reduction. As discussed in section 3.1 the formation of oxygen interstitials is at least one of the reasons why La-doped $Ba_3In_2O_6$ remains insulating. Superconductivity in nickelates, which was recently discovered, is not observed without prior topotactic reduction of the epitaxial films [65, 66]. Thus, we assess whether reduction of the films may induce superconductivity in 20% La-doped $Ba_3In_2O_6$ by either decreasing or completely annihilating the oxygen interstitials. To this end, reductions are performed on such a sample without a capping layer using a thermal atomic hydrogen source [67, 68] with the same setup described in [69]. Three successive reductions are performed. Reduction 1: nominal atomic H-flux 2.1×10^{15} at cm^{-2} s^{-1}, temperature

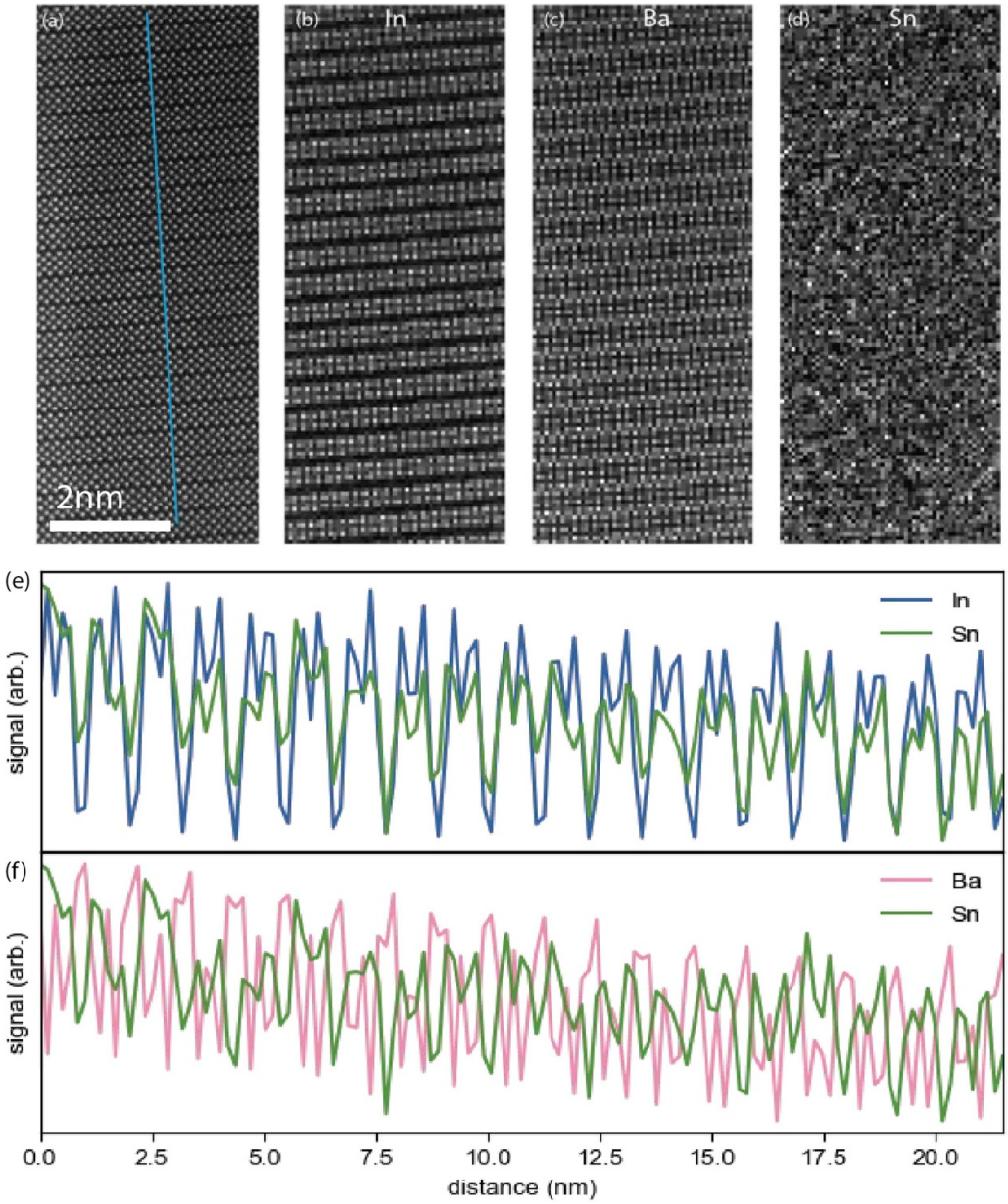

Figure 7. (a) A wider field of view of the HAADF-STEM image of the sample shown in figure 6(c). (b)–(d) Four times binned elemental maps obtained by EDX for (b) the In-L, In-K_α, and In-K_β edges, (c) the Ba-L, and Ba-K_α edges, and (d) the Sn-L and Sn-K_α edges. (e)–(f) Line profiles calculated for the blue line in (a) comparing the Sn signal to the (e) In signal and (f) Ba signal. The line profiles indicate that Sn occupies the In and not the Ba sites.

300 °C, time 10 min. Reduction 2: nominal atomic H-flux 2.3×10^{15} at cm^{-2} s^{-1}, temperature 500 °C, time 30 min. Reduction 3: 2.3×10^{15} at cm^{-2} s^{-1}, temperature 750 °C, time 20 min. In this experimental setup the structure of the 20% La-doped $Ba_3In_2O_6$ can be measured in situ using RHEED. However, no substantial changes to the sample surface were apparent following the three reductions and the original structure was maintained throughout the experiment. Following each of the subsequent reduction attempts, the sample is cooled in vacuum ($\leqslant 2 \times 10^{-9}$ Torr) to well below 100 °C before brief exposure to air and measurement of the sample resistance. However, no measurable conductivity was detected after any of the reductions ($R \geqslant 50$ MΩ).

3.3.2. Surface alkali doping. *In-situ* surface alkali doping has previously successfully been applied to induce superconductivity in several different material systems [70–74]. To characterize the electric properties of the film, we perform in-situ resistivity measurements using a custom-built UHV four-point transport probe with a base pressure of 7×10^{-11} Torr. The uncapped, undoped film expectedly shows highly insulating behavior, exceeding the measurement limit of our electronics for temperatures below 270 K. While being maintained in UHV at 50 K, we sequentially deposit Cs adatoms in steps of 0.1 ML, up to a total nominal coverage of 2 ML. Unfortunately, no deviation from the low temperature insulating behavior is observed, as the film resistance remains

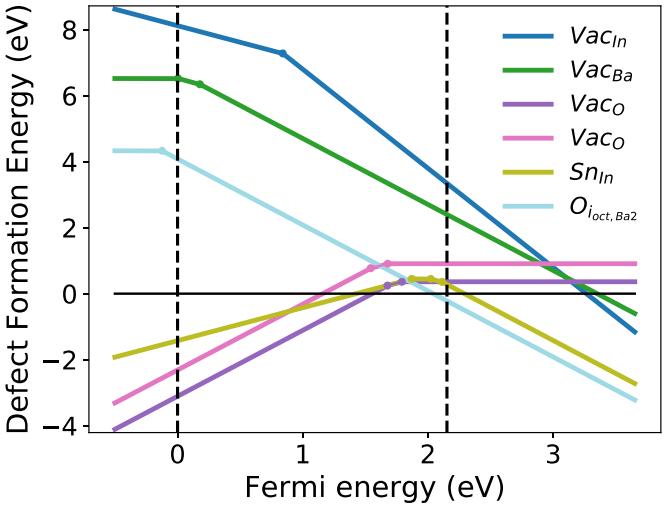

Figure 8. Dependence of the defect formation energy on the Fermi energy for cation-rich and oxygen-poor growth conditions obtained by HSE computations for Sn-doping. Violet represents the oxygen vacancy formation in the rock salt layers and pink in the single layers. Green represents Ba vacancies, dark blue In vacancies, and light blue the formation of oxygen interstitials. The substitution of Sn for In is shown in light green.

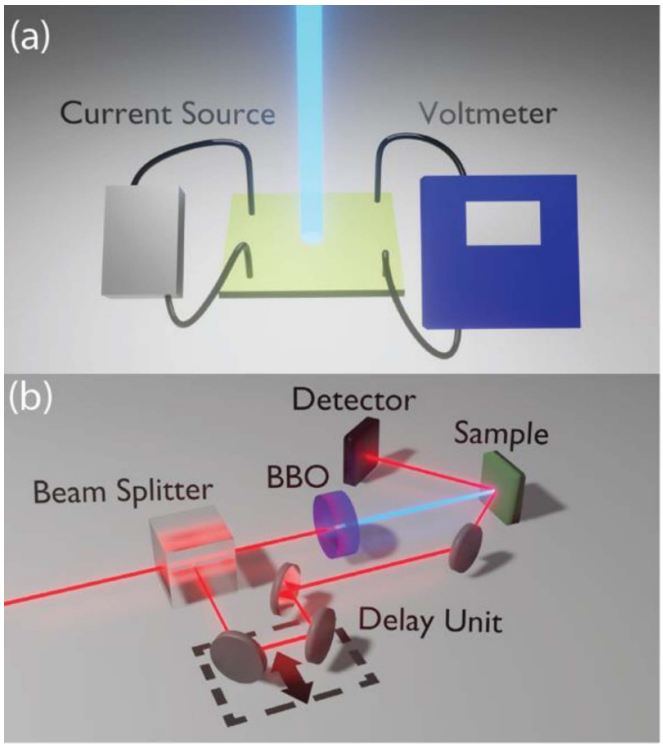

Figure 9. (a) Setup for measuring conductivity changes in van-der-Pauw geometry resulting from photoexcitation by a continuous wave laser. (b) Apparatus for the pump-probe experiment. The laser produces 800 nm, 35 fs laser pulses, which are split at a 90/10 beam splitter to serve as pump and probe, respectively. The pump beam is converted to 400 nm through an SHG process in a β-BaB_2O_4 (BBO) crystal. The probe beam is delayed in time using a mechanical stage and directed to the sample at an oblique incidence. The intensity of the reflected beam is measured in a photodetector. Changes in the reflected intensity are monitored through a lock-in amplifier.

consistently above the measurement impedance limit of our electronics.

3.3.3. Optical pumping. Photo-induced superconductivity is a relative new development enabled by advances in laser technology allowing for the generation of precisely shaped strong-field pulses at THz frequencies [75]. Thus far the technique has proven especially successful for superconductivity in cuprates [76, 77]. To attempt photo-induced superconductivity in $Ba_3In_2O_6$ the sample is bonded and its resistivity is measured in van-der-Pauw geometry. As expected, the initial resistance is large ($\geqslant$100 GΩ). Nevertheless, resonantly pumping the sample with 405 nm 50 mW laser, and an incident diameter of 1.4 mm is attempted. No change of resistance independent of the beam position on the sample is observed (figure 9(a)). We further optically monitored the resistance change by measuring the transient reflectivity. If resonantly pumping changes the electronic occupation, the reflectivity of the sample is expected to change. To this end a 1 kHz, 800 nm, 35 fs pulsed laser is utilized with a β-BaB_2O_4 crystal to convert the 800 nm pump pulses to 400 nm pulses. We chopped the pump at 500 Hz and use a synchronized lock-in amplifier to measure the change in reflectivity of the sample induced by the pump pulses. The setup is depicted in figure 9(b). Temporal overlap is guaranteed on a highly reactive test sample before probing the $Ba_3In_2O_6$ sample. Using fluences up to 10 mJ cm^{-2}, no substantial change in reflectivity at or after the temporal overlap is observed. This indicates that the system is not responsive to pumping with 400 nm light.

3.3.4. Liquid ion gating. Liquid ion gating has proven to be a valuable tool for achieving or enhancing superconductivity in various oxides [78–80]. Applying it successfully, however, requires a conducting backside electrode. Thus far the epitaxial growth of $Ba_3In_2O_6$ has solely been demonstrated on insulating substrates, i.e. (001) MgO and (001) $SrTiO_3$ [14]. We, thus, attempt an epitaxial growth of $Ba_3In_2O_6$ on a 30 nm epitaxial film of $SrRuO_3$ on (001) $SrTiO_3$ [23]. Attempts to grow epitaxial $SrRuO_3$ on (001) MgO were unsuccessful. Figure 10 shows the θ–2θ-scan of a 120 nm $Ba_3In_2O_6$/ 30 nm $SrRuO_3$/ (001) $SrTiO_3$ sample. The diffraction pattern shows that the bilayer consists of the intended epitaxial phases with no detected impurity phases. The crystalline quality is similar to $Ba_3In_2O_6$ films grown on (001) $SrTiO_3$, which is impressive considering the high temperatures needed for the growth of the $Ba_3In_2O_6$ layer [14]. Epitaxial $Ba_3In_2O_6$ with a conducting $SrRuO_3$ backside electrode allows us to probe for superconductivity by liquid-ion gating. For that the films are patterned into 900 $\times$ 100 μm^2 Hall bar devices. Hydrated polyethylene glycol and N,N-diethyl-N-methyl-N-(2-methoxyethyl)ammoniumbis(trifluoromethylesulfonyl)imide are tried as electrolytes over a wide temperature range with gate voltages of up to $\pm$3 V. In this parameter space no signs of superconductivity were detectable (supplementary figure 7).

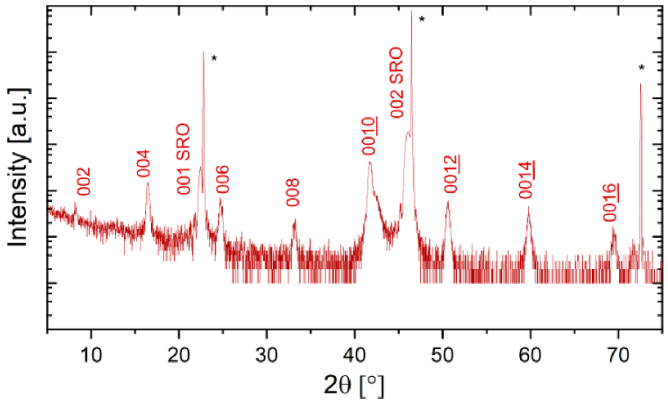

Figure 10. θ–2θ diffraction pattern of a 120 nm $Ba_3In_2O_6$/30 nm $SrRuO_3$/(001) $SrTiO_3$ sample. Asterisks mark the $SrTiO_3$ substrate peaks. SRO marks the $SrRuO_3$ peaks. The peaks of $Ba_3In_2O_6$ indicate a crystal quality comparable to growth on $SrTiO_3$ [14].

4. Discussion

In this paper we want to answer two questions. The main question is if $Ba_3In_2O_6$ is a high-T_c superconductor. Additionally, as this prediction was made recently by machine learning [7], we also consider this an initial trial of whether the prediction of superconductivity by this new approach is more successful in comparison to more traditional means of predicting materials properties. To this end we probed the material by various experimental and theoretical methods and tried various strategies to induce superconductivity, the results of which were presented in section 3. Here these results are discussed comprehensively.

While we attempted to induce superconductivity through various strategies, the failure of each of them is linked to the same fundamental issue of $Ba_3In_2O_6$. $Ba_3In_2O_6$ has a comparably wide bandgap of ≈2.8 eV, which is in stark contrast to what is desired for superconductivity [81]. Additionally a wide bandgap makes in general electronic doping more difficult as it increases the chance of deep dopants (>0.2 eV below the conduction band), which do not contribute significant amounts of electrons. However, In-based oxide with large band gaps such as In_2O_3 can be highly doped. Interestingly, finding a shallow donor is not the central issue for the two dopants discussed in depth here. The issue for both is linked to the crystal structure of $Ba_3In_2O_6$ and to the 5-fold coordination of In (see figure 1). This leaves a site that can be readily filled by oxygen interstitials, which compensate electron doping. 5-fold coordinated In^{3+} is rare in oxides and In^{3+} favors in the vast majority of the case an octahedral 6-fold coordination [82]. We observe these oxygen interstitials experimentally. Likely, oxygen interstitials will be equally problematic for other electron doping attempts. The 5-fold coordination of In is also a probable explanation for the stabilization of the lower and less stable 2+ oxidation state of Sn through the lone-pair effect [83]. This potentially rules out doping by other elements, for which the lower oxidation state can be stabilized in the same manner [84], and for which the lower oxidation state is not a suitable electron donor. They may constitute a promising approach for p-type doping if the resulting defect states are less deep.

Considering these findings, inducing superconductivity in $Ba_3In_2O_6$ seems unlikely as the formation of the oxygen interstitial will always compensate the donated electrons. A few more dopants explored computationally: F_O and Zr_{In} show respectively a shallow donor and a deep donor (as shown in supplementary figure 8). F_O appears, however, not more shallow than La_{Ba} or In_{Sn}. The oxygen interstitial compensation problem will only be addressed if very reducing conditions are applied which might be difficult while keeping the $Ba_3In_2O_6$ phase. Our computations indicate that this could be achieved only if going to non-equilibrium conditions.

The most promising route may be to induce p-type conductivity even though our results indicate that it will be difficult to find a shallow defect state. The isostructural known high-T_c superconductor $La_2SrCu_2O_6$ is also based on p-type conductivity and here oxygen interstitials add holes. Unfortunately, the large bandgap of $Ba_3In_2O_6$ makes it an insulator and the energy level of oxygen interstitials are too deep to induce p-type conductivity.

$Ba_3In_2O_6$ is, of course, a very isolated case to consider for a superconductor predicted by machine learning. For this specific case our verdict is that machine learning is not more successful than the traditional means of predicting materials properties for identifying new superconductors. Nonetheless, utilizing machine learning to predict high-T_c superconductors is still a comparably new approach and is constantly being improved [8, 85–87]. Our work indicates that bringing factors that are readily computable with first-principles computations such as band gap and the energetics of doping into these superconductor predictions would be helpful in the selection of the most promising systems in which high T_c superconductivity might be experimentally realized. It may well be that $Ba_3In_2O_6$ is a potential theoretical superconductor but that the carrier level needed can never be achieved. At this point novel superconducting materials (and other materials of interest) are being suggested at a speed greatly exceeding the ability of experimentalists to synthesize and thoroughly probe these materials. It will be exciting to see if novel trends in the epitaxial deposition of materials will help close this speed gap between theoretical prediction and experimental validation (or refutation) to some extent [16].

5. Conclusion

Already in the 1980s $Ba_3In_2O_6$ was suspected of being a high-T_c superconductor due to its structure [2]. More recently this suspicion was raised again by machine learning predictions [7]. Unfortunately, the hygroscopic behavior of $Ba_3In_2O_6$ previously impeded its thorough characterization. Utilizing the recent progress in epitaxially growing and stabilizing $Ba_3In_2O_6$ [14] we are able to probe the electronic structure of $Ba_3In_2O_6$ and compare it to first principles calculations.

We find $Ba_3In_2O_6$ to be highly insulating, which is not surprising given that we determine its bandgap to be relatively wide (experimentally ≈ 2.8 eV, first principles ≈ 2.15 eV).

The wide bandgap makes doping difficult due to the increased probability of deep defects. Additionally, we find the 5-fold coordination of In to result in interesting effects that regrettably also counter electron dopability. The In 5-fold coordination leaves an easy site for oxygen interstitials to form, which are also observed experimentally by ABF-STEM. Oxygen interstitials compensate the electron doping by, e.g. La. The 5-fold coordinated In site also stabilizes the lower 2+ oxidation state of Sn as a dopant through the lone pair effect. Other strategies of inducing superconductivity such as alkali surface doping, optical pumping, and liquid ion gating prove equally futile. At this point we conclude that it is highly unlikely, but not necessarily impossible, to induce superconductivity in $Ba_3In_2O_6$.

The ability of $Ba_3In_2O_6$ to accommodate significant concentrations of oxygen interstitials, however, makes it an interesting material for catalysis applications. In fact, it was recently predicted as a promising photocatalyst for solar-to-hydrogen conversion [88].

This case study also provides valuable feedback for new machine learning strategies. Combining machine learning results with easily computable properties such as band gap and doping may yield more reliable results—making the prediction of high-T_c superconductors tangible.

Data availability statements

The data that support the findings of this study are openly available at the following URL/DOI: 10.34863/xg24-bj80.

Acknowledgments

The authors thank Jochen Mannhart for critical reading, support, and discussions. F V E H, M A S, V S, C T P, G K, M B, K M S, B F, L F K, and D G S acknowledge support from the National Science Foundation [Platform for the Accelerated Realization, Analysis, and Discovery of Interface Materials (PARADIM)] under Cooperative Agreement No. DMR-2039380. Substrate preparation was performed in part at the Cornell NanoScale Facility, a member of the National Nanotechnology Coordinated Infrastructure (NNCI), which is supported by the National Science Foundation (Grant No. NNCI-2025233). This work made use of the Cornell Center for Materials Research Shared Facilities, which are supported through the NSF MRSEC program (DMR-1719875). M A S acknowledges additional support from the NSF GRFP under Award No. DGE-2139899. This research was funded in part by the Gordon and Betty Moore Foundation's EPiQS Initiative through Grant No. GBMF9073 to Cornell University. The theoretical part of this work was supported by the U.S. Department of Energy, Office of Science, Basic Energy Sciences under award number DE-SC0023509. This research used resources of the National Energy Research Scientific Computing Center (NERSC), a DOE Office of Science User Facility supported by the Office of Science of the U.S. Department of Energy under contract no. DE-AC02-05CH11231 using NERSC award BES-ERCAP0023830. Electrolyte gating experiments at Brookhaven National Laboratory were funded by the US Department of Energy, Office of Science, Materials Science and Engineering Division.

ORCID iDs

F V E Hensling https://orcid.org/0000-0003-3852-7214
M A Smeaton https://orcid.org/0000-0001-9114-1009
B Shrestha https://orcid.org/0009-0002-3293-2542
V Show https://orcid.org/0000-0002-5700-0429
C T Parzyck https://orcid.org/0000-0002-3835-7115
C Hennighausen https://orcid.org/0000-0003-1829-0600
G-M Rignanese https://orcid.org/0000-0002-1422-1205
I Subedi https://orcid.org/0000-0003-2300-6010
A S Disa https://orcid.org/0000-0002-7762-3244
A T Bollinger https://orcid.org/0000-0002-3629-6611
G Hautier https://orcid.org/0000-0003-1754-2220

References

[1] Onnes H K 1911 The superconductivity of mercury *Commun. Phys. Lab. Univ. Leiden* **122** 122–4
[2] Bednorz J G and Mueller K A 1986 Possible highT c superconductivity in the Ba-La-Cu-O system *Z. Phys.* B **64** 189–93
[3] Matthias B T 1970 The empirical approach to superconductivity *Applied Solid State Physics* (Springer) pp 179–88
[4] Matthias B T 1970 High-temperature superconductivity? *Solid State Phys.* **3** 93–96
[5] Matthias B T 1973 *Tc's—The High and Low of It, the Science and Technology of Superconductivity* ed W D Gregory, W N Mathews and E A Edelsack (Springer) pp 7823–30
[6] Curtarolo S, Hart G L W, Nardelli M B, Mingo N, Sanvito S and Levy O 2013 The high-throughput highway to computational materials design *Nat. Mater.* **12** 191–201
[7] Liu Z-L, Kang P, Zhu Y, Liu L and Guo H 2020 Material informatics for layered high- T C superconductors *APL Mater.* **8** 061104
[8] Roter B and Dordevic S V 2020 Predicting new superconductors and their critical temperatures using machine learning *Physica* C **575** 1353689
[9] Pereti C, Bernot K, Guizouarn T, Laufek F, Vymazalová A, Bindi L, Sessoli R and Fanelli D 2023 From individual elements to macroscopic materials: in search of new superconductors via machine learning *npj Comput. Mater.* **9** 1–9
[10] Mader K and Müller-Buschbaum H 1988 Zur Kristallstruktur von $Ba_3In_2O_6$ *Z. Anorg. Allg. Chem.* **559** 89–94
[11] Cava R J *et al* 1990 Superconductivity at 60 K in La_2-xSrxCaCu$_2O_6$: the simplest double-layer cuprate *Nature* **345** 602–4
[12] Tsukada I, Nagao Y and Ando Y 2004 In situ epitaxial growth of superconducting La-based bilayer cuprate thin films *Phys. Rev.* B **69** 1–4
[13] Kwestroo W, van Gerven H C A and Langereis C 1977 Compounds in the system BaO-In2O3 *Mater. Res. Bull.* **12** 157–60

[14] Hensling F V E, Smeaton M A, Show V, Azizie K, Barone M R, Kourkoutis L F and Schlom D G 2022 Epitaxial growth of the first two members of the $Ba_{n+1}In_nO_{2.5n+1}$ Ruddlesden–Popper homologous series *J. Vac. Sci. Technol.* A **40** 062707

[15] Antipov E, Lykova L and Kovba L 1990 Crystalline-structure of $BA_3IN_2O_6$ *Koord. Khim.* **16** 770–2

[16] Hensling F V E, Braun W, Kim D Y, Majer L N, Smink S, Faeth B and Mannhart J 2024 State of the art, trends, and opportunities for oxide epitaxy *APL Mater.* **12**

[17] Vogt P, Schlom D G, Hensling F V E, Azizie K, Liu Z K and Bocklund B J 2020 Suboxide molecular beam epitaxy and related structures *U.S. Patent* 0122843

[18] Wang C P, Do K B, Beasley M R, Geballe T H and Hammond R H 1997 Deposition of in-plane textured MgO on amorphous Si_3N_4 substrates by ion-beam-assisted deposition and comparisons with ion-beam-assisted deposited yttria-stabilized-zirconia *Appl. Phys. Lett.* **71** 2955–7

[19] Arendt P N and Foltyn S R 2004 Biaxially textured IBAD-MgO templates for YBCO-coated conductors *MRS Bull.* **29** 543–50

[20] Xiong X, Kim S, Zdun K, Sambandam S, Rar A, Lenseth K P and Selvamanickam V 2009 Progress in high throughput processing of long-length, high quality, and low cost IBAD MgO buffer tapes at superpower *IEEE Trans. Appl. Supercond.* **19** 3319–22

[21] MacManus-Driscoll J L and Wimbush S C 2021 Processing and application of high-temperature superconducting coated conductors *Nat. Rev. Mater.* **6** 587–604

[22] Molodyk A *et al* 2021 Development and large volume production of extremely high current density $YBa_2Cu_3O_7$ superconducting wires for fusion *Sci. Rep.* **11** 1–11

[23] Nair H P *et al* 2018 Synthesis science of $SrRuO_3$ and $CaRuO_3$ epitaxial films with high residual resistivity ratios *APL Mater.* **6** 046101

[24] Adkison K M, Shang S-L, Bocklund B J, Klimm D, Schlom D G and Liu Z-K 2020 Suitability of binary oxides for molecular-beam epitaxy source materials: a comprehensive thermodynamic analysis *APL Mater.* **8** 081110

[25] Sun J *et al* 2022 Canonical approach to cation flux calibration in oxide molecular-beam epitaxy *Phys. Rev. Mater.* **6** 033802

[26] Koster G, Kropman B L, Rijnders G J H M, Blank D H A and Rogalla H 1998 Quasi-ideal strontium titanate crystal surfaces through formation of strontium hydroxide *Appl. Phys. Lett.* **73** 2920–2

[27] Koster G, Rijnders G, Blank D H A and Rogalla H 2000 Surface morphology determined by (0 0 1) single-crystal $SrTiO_3$ termination *Physica* C **339** 215–30

[28] Lee J, Rovira P I, An I and Collins R W 1998 Rotating-compensator multichannel ellipsometry: applications for real time Stokes vector spectroscopy of thin film growth *Rev. Sci. Instrum.* **69** 1800–10

[29] Woollam J A, Johs B D, Herzinger C M, Hilfiker J N, Synowicki R A and Bungay C L 1999 Overview of variable-angle spectroscopic ellipsometry (VASE): i. basic theory and typical applications *Proc. SPIE* **10294** 1029402

[30] Alterovitz S A and Johs B 1998 Multiple minima in the ellipsometric error function *Thin Solid Films* **313–314** 124–7

[31] Collins R W and Ferlauto A S 2006 Optical physics of materials *ChemInform* **37** 125

[32] Aspnes D E 1980 Handbook on semiconductors *Handbook on Semiconductors* ed M Balkanski (North-Holland) p 109

[33] Jellison G E and Modine F A 1996 Parameterization of the optical functions of amorphous materials in the interband region *Appl. Phys. Lett.* **69** 371–3

[34] Junda M M, Grice C R, Yan Y and Podraza N J 2019 Parametric optical property database for CdSe1−xSx alloys *Electron. Mater. Lett.* **15** 500–4

[35] Oldham W G 1969 Numerical techniques for the analysis of lossy films *Surf. Sci.* **16** 97–103

[36] Tauc J, Grigorovici R and Vancu A 1966 Optical properties and electronic structure of amorphous germanium *Phys. Status Solidi* **15** 627–37

[37] Blöchl E 1994 Projector augmented-wave method *Phys. Rev.* B **50** 17953–79

[38] Kresse G and Furthmüller J 1996 Efficiency of ab-initio total energy calculations for metals and semiconductors using a plane-wave basis set *Comput. Mater. Sci.* **6** 15–50

[39] Kresse G and Furthmüller J 1996 Efficient iterative schemes for ab initio total-energy calculations using a plane-wave basis set *Phys. Rev.* B **54** 11169–86

[40] Freysoldt C, Neugebauer J and Van de Walle C G 2011 Electrostatic interactions between charged defects in supercells *Phys. Status Solidi* **248** 1067–76

[41] Broberg D, Medasani B, Zimmermann N E R, Yu G, Canning A, Haranczyk M, Asta M and Hautier G 2018 PyCDT: a Python toolkit for modeling point defects in semiconductors and insulators *Comput. Phys. Commun.* **226** 165–79

[42] Heyd J, Scuseria G E and Ernzerhof M 2003 Hybrid functionals based on a screened Coulomb potential *J. Chem. Phys.* **118** 8207–15

[43] Lyons J L and Van De Walle C G 2017 Computationally predicted energies and properties of defects in GaN *npj Comput. Mater.* **3** 1–9

[44] Zhang S and Northrup J 1991 Chemical potential dependence of defect formation energies in GaAs: application to Ga self-diffusion *Phys. Rev. Lett.* **67** 2339–42

[45] Komsa H P, Rantala T T and Pasquarello A 2012 Finite-size supercell correction schemes for charged defect calculations *Phys. Rev.* B **86** 1–16

[46] Hensling F V E *et al* 2021 Epitaxial stannate pyrochlore thin films: limitations of cation stoichiometry and electron doping *APL Mater.* **9** 051113

[47] Kumagai Y and Oba F 2014 Electrostatics-based finite-size corrections for first-principles point defect calculations *Phys. Rev.* B **89** 195205

[48] Ghosh G 1997 *Handbook of Optical Constants of Solids* ed E Palik (Elsevier)

[49] Tan G L, Lemon M F, Jones D J and French R H 2005 Optical properties and London dispersion interaction of amorphous and crystalline SiO_2 determined by vacuum ultraviolet spectroscopy and spectroscopic ellipsometry *Phys. Rev.* B **72** 205117

[50] Bakos T 2003 *Defects in Amorphous SiO_2: Reactions, Dynamics and Optical Properties* (Vanderbilt University)

[51] Chan M K Y and Ceder G 2010 Efficient band gap prediction for solids *Phys. Rev. Lett.* **105** 5–8

[52] Nie Y F, Di Sante D, Chatterjee S, King P D C, Uchida M, Ciuchi S, Schlom D G and Shen K M 2015 Formation and observation of a quasi-two-dimensional dxy electron liquid in epitaxially stabilized Sr_2-xLaxTiO$_4$ thin films *Phys. Rev. Lett.* **115** 1–5

[53] Shin S S, Yeom E J, Yang W S, Hur S, Kim M G, Im J, Seo J, Noh J H and Seok S 2017 Colloidally prepared La-doped $BaSnO_3$ electrodes for efficient, photostable perovskite solar cells *Science* **356** 167–71

[54] Paik H *et al* 2017 Adsorption-controlled growth of La-doped $BaSnO_3$ by molecular-beam epitaxy *APL Mater.* **5** 116107

[55] Shannon R D 1976 Revised effective ionic radii and systematic studies of interatomic distances in halides and chalcogenides *Acta Crystallogr.* A **32** 751–67

[56] Krockenberger Y, Kurian J, Winkler A, Tsukada A, Naito M and Alff L 2008 Superconductivity phase diagrams for the

electron-doped cuprates R2-x Cex Cu O_4 (R=La, Pr, Nd, Sm, and Eu) *Phys. Rev.* B **77** 2–5
[57] Sleight A W, Gillson J L and Bierstedt P E 1975 High-temperature superconductivity in the BaPb1-xBixO_3 system *Solid State Commun.* **17** 27–28
[58] Kazakov S M, Chaillout C, Bordet P, Capponi J J, Nunez-Regueiro M, Rysak A, Tholence J L, Radaelli P G, Putilin S N and Antipov E V 1997 Discovery of a second family of bismuth-oxide-based superconductors *Nature* **390** 148–9
[59] Zheng X *et al* 2020 Synthesis, structure, and superconductivity of B-site doped perovskite bismuth lead oxide with indium *Inorg. Chem. Front.* **7** 3561–70
[60] Bierwagen O 2015 Indium oxide—A transparent, wide-band gap semiconductor for (opto)electronic applications *Semicond. Sci. Technol.* **30** 24001
[61] Uchida S, Takagi H and Tokura Y 1989 Doping effect on the transport and optical properties of P-type and N-type cuprate superconductors *Physica C* **162–164** 1677–80
[62] Choisnet J, Bizo L, Retoux R and Raveau B 2004 Antimony and antimony-tin doped indium oxide, IAO and IATO: promising transparent conductors *Solid State Sci.* **6** 1121–3
[63] Li X, Zhang Q, Miao W, Huang L and Zhang Z 2006 Transparent conductive oxide thin films of tungsten-doped indium oxide *Thin Solid Films* **515** 2471–4
[64] Seth M, Faegri K and Schwerdtfeger P 1998 The stability of the oxidation state +4 in group 14 compounds from carbon to element 114 *Angew. Chem., Int. Ed.* **37** 2493–6
[65] Li D, Lee K, Wang B Y, Osada M, Crossley S, Lee H R, Cui Y, Hikita Y and Hwang H Y 2019 Superconductivity in an infinite-layer nickelate *Nature* **572** 624–7
[66] Wei W, Vu D, Zhang Z, Walker F J and Ahn C H 2023 Superconducting Nd1-xEuxNiO_2 thin films using in situ synthesis *Sci. Adv.* **9** 2–7
[67] Tschersich K G and Von Bonin V 1998 Formation of an atomic hydrogen beam by a hot capillary *J. Appl. Phys.* **84** 4065–70
[68] Tschersich K G, Fleischhauer J P and Schuler H 2008 Design and characterization of a thermal hydrogen atom source *J. Appl. Phys.* **104** 034908
[69] Parzyck C T, Anil V, Wu Y, Goodge B H, Roddy M, Kourkoutis L F, Schlom D G and Shen K M 2024 Synthesis of thin film infinite-layer nickelates by atomic hydrogen reduction: clarifying the role of the capping layer *APL Mater.* **12** 031131
[70] Hossain M A *et al* 2008 In situ doping control of the surface of high-temperature superconductors *Nat. Phys.* **4** 527–31
[71] Han T T, Chen L, Cai C, Wang Z G, Wang Y D, Xin Z M and Zhang Y 2021 Metal-insulator transition and emergent gapped phase in the surface-doped 2D semiconductor 2H−$MoTe_2$ *Phys. Rev. Lett.* **126** 106602
[72] Li Q, Lv Y, Xu Y, Zhu L, Zhao W, Chen Y and Li S-C 2022 Surface electron doping induced double gap opening in T d -WTe 2 *Chin. Phys.* B **31** 066802
[73] Parzyck C T, Faeth B D, Tam G N, Stewart G R and Shen K M 2020 Enhanced surface superconductivity in Ba(Fe0.95Co0.05)2As2 *Appl. Phys. Lett.* **116** 0–5
[74] Faeth B D, Yang S L, Kawasaki J K, Nelson J N, Mishra P, Parzyck C T, Li C, Schlom D G and Shen K M 2021 Incoherent cooper pairing and pseudogap behavior in single-layer FeSe/SrTi O_3 *Phys. Rev.* X **11** 1–11
[75] Cavalleri A 2018 Photo-induced superconductivity *Contemp. Phys.* **59** 31–46
[76] Fausti D, Tobey R I, Dean N, Kaiser S, Dienst A, Hoffmann M C, Pyon S, Takayama T, Takagi H and Cavalleri A 2011 Light-induced superconductivity in a stripe-ordered cuprate *Science* **331** 189–91
[77] Kaiser S *et al* 2014 Optically induced coherent transport far above Tc in underdoped YBa_2 Cu_3 $O_{6+\delta}$ *Phys. Rev.* B **89** 184516
[78] Ye J T, Inoue S, Kobayashi K, Kasahara Y, Yuan H T, Shimotani H and Iwasa Y 2010 Liquid-gated interface superconductivity on an atomically flat film *Nat. Mater.* **9** 125–8
[79] Rafique M, Feng Z, Lin Z, Wei X, Liao M, Zhang D, Jin K and Xue Q 2019 Ionic liquid gating induced protonation of electron-doped cuprate superconductors *Nano Lett.* **19** 7775–80
[80] Ren T *et al* 2022 Two-dimensional superconductivity at the surfaces of $KTaO_3$ gated with ionic liquid *Sci. Adv.* **8** 1–6
[81] Pickett W E 1989 Electronic structure of the high-temperature oxide superconductors *Rev. Mod. Phys.* **61** 433–512
[82] Waroquiers D *et al* 2017 Statistical analysis of coordination environments in oxides *Chem. Mater.* **29** 8346–60
[83] Fabini D H *et al* 2016 Dynamic stereochemical activity of the Sn2+ lone pair in perovskite CsSnBr3 *J. Am. Chem. Soc.* **138** 11820–32
[84] Walsh A, Payne D J, Egdell R G and Watson G W 2011 Stereochemistry of post-transition metal oxides: revision of the classical lone pair model *Chem. Soc. Rev.* **40** 4455–63
[85] Matsumoto K and Horide T 2019 An acceleration search method of higher Tc superconductors by a machine learning algorithm *Appl. Phys. Express* **12** 10–14
[86] Konno T, Kurokawa H, Nabeshima F, Sakishita Y, Ogawa R, Hosako I and Maeda A 2021 Deep learning model for finding new superconductors *Phys. Rev.* B **103** 1–6
[87] Yazdani-Asrami M 2023 Artificial intelligence, machine learning, deep learning, and big data techniques for the advancements of superconducting technology: a road to smarter and intelligent superconductivity *Supercond. Sci. Technol.* **36** 084001
[88] Gelin S *et al* 2024 Ternary oxides of s- and p-block metals for photocatalytic solar-to-hydrogen conversion *PRX Energy* **3** 1